

## Oxidation kinetics and mechanisms of Ni-base alloys in pressurised water reactor primary conditions: Influence of subsurface defects

**HÉLÈNE LEFAIX-JEULAND<sup>(1,2)</sup>, LOÏC MARCHETTI<sup>(1)</sup>, STÉPHANE PERRIN<sup>(1)\*</sup>, MICHÈLE PIJOLAT<sup>(3)</sup>, MOHAMMED SENNOUR<sup>(4)</sup>, RÉGINE MOLINS<sup>(4)</sup>**

<sup>(1)</sup> CEA Saclay, DEN/DPC/SCCME, Laboratoire d'Etude de la Corrosion Aqueuse, 91191 Gif-sur-Yvette, France

<sup>(2)</sup> CEA, DEN/DMN, Service de Recherches en Métallurgie Physique, 91191 Gif-sur-Yvette, France

<sup>(3)</sup> Ecole Nationale Supérieure des Mines de Saint Etienne, Centre SPIN ; Département PRESSIC ; LPMG -UMR CNRS 5148, 158 Cours Fauriel ; 42023 Saint-Étienne Cedex 2, France

<sup>(4)</sup> MINES, ParisTech, Centre des Matériaux, UMR CNRS 7633, B.P. 87, 91003 Evry Cedex, France

### Abstract

Oxidation of Alloy 690 in PWR primary water conditions has been investigated, considering particularly the role played by subsurface structural defects. To simulate a defective surface state, Xe implantation has been set up on samples. Corrosion experiments were thereafter performed in a corrosion loop simulating the PWR medium with durations between 24 h and 1000 h. Microstructural observations and NRA measurements underlined the role played by defects on the crystallinity of the continuous oxide spinel layer, on the nucleation of Cr<sub>2</sub>O<sub>3</sub> nodules and on the oxidation rate. The higher defects concentration seemed to modify the oxygen diffusion in the oxide scale.

### Highlights

- ~ Ni-base alloy uniform corrosion in primary medium of Pressurised Water Reactor.
- ~ Influence of alloy subsurface defects created by ion implantation on oxide layer.
- ~ Defects in the alloy modify the crystallinity and the nucleation rate of the oxides.
- ~ These modifications are linked to the change of oxidation kinetic curves.

### Keywords:

*Oxidation; Alloy; Ion implantation; Kinetic parameters; TEM; SIMS*

### I. Introduction

Knowledge of the oxidation processes on Ni alloys in Pressurised Water Reactors (PWR) coolant is of major importance for at least two practical reasons:

- (i) the radioactivity of the primary circuit is primarily due to cations released by corrosion of the steam generator tubes and
- (ii) the oxidation process is important in the mechanisms of the initiation of intergranular stress corrosion cracking in Alloys 600, 82 and 182.

---

\* Corresponding Author: [steph.perrin@cea.fr](mailto:steph.perrin@cea.fr)

In previous papers, we investigated properties of the oxide layers formed on nickel-based alloys in PWR primary medium by transmission electron microscopy (TEM) [1] as well as by photoelectrochemical techniques [2]. These studies enabled to propose an oxide layer divided into two major parts. First, the external layer was composed of a nickel ferrite ( $\text{Ni}_{(1-z)}\text{Fe}_{(2+z)}\text{O}_4$ ) and nickel hydroxide. It was also highlighted in Reference [1] that the formation of this external scale was due to precipitation phenomena. Next, the internal layer was mainly composed of a continuous spinel layer, which was a mixed iron and nickel chromite ( $\text{Ni}_{(1-x)}\text{Fe}_x\text{Cr}_2\text{O}_4$ ). Moreover, nodules of  $\text{Cr}_2\text{O}_3$ , with a size about 5 nm, were uniformly distributed at the interface between this internal spinel layer and the alloy. No chromium depletion was observed in the alloy, at the alloy/oxide interface.

Nevertheless, in previous works [3], [4], [5] and [6], a chromium depleted zone was observed beneath the oxide scale, in Ni-base alloys exposed to PWR primary conditions. For some of them [3], [4] and [6], the presence of this chromium depleted layer was concomitant with a disturbed microstructure characterised by small grains of alloy and a strong dislocation density.

Carrette [3] studied more particularly by TEM the influence of the work hardening rate on the internal oxide thickness in PWR primary conditions. These results showed that the thicknesses of the oxide layer and the chromium depleted layer in the alloy increased with the cold working. On electropolished samples, the oxide layer observed was not continuous and no chromium depleted layer was observed.

Although these works seem to show that cold work had an effect on the oxide layer as well as on the alloy beneath this oxide scale, this effect has never been clearly studied in terms of:

- (i) the nature and the structure of the oxide film and
- (ii) its oxide growth kinetics.

It has also been established that cold working enhanced corrosion rates [3], [7] and [8]. In addition to the oxide scale changes, the cations release kinetics, continuously measured, strongly depended on cold working [3], [8] and [9]. For example, the suppression of this surface cold working by an electropolishing treatment leads to a strong reduction of the release process.

Therefore, these results show the key role of the alloy surface defects on the oxide layer, on the corrosion as well as the release kinetics for Ni-base alloys exposed to PWR primary medium. The aim of this paper is to further explain this effect based on a better understanding of the oxidation mechanism and growth kinetics. Ion implantation method, well-known to provoke structural damages in materials, has been used to simulate different surface states in Alloy 690. Three complementary methods were then used to study effects of these defects on the corrosion process:

- (i) Scanning Electron Microscopy (SEM) and Transmission Electron Microscopy (TEM) observations in order to identify the structural modifications in the oxide layer;
- (ii) Sequenced oxidation with  $\text{H}_2(^{18}\text{O})$  and Secondary Ion Mass Spectroscopy (SIMS) analysis in order to underline the consequence of these defects on the diffusion process in the oxide;
- (iii) Oxide thickness measurement by Nuclear Reaction Analysis (NRA) in order to study the oxidation kinetics

## II. Material and methods

### II.1. Materials

The composition of Alloy 690 used in this study is given in Table 1. Coupons (30mm × 20mm × 2.5mm) were mechanically mirror-polished with SiC paper up to grade 1200, diamond

paste up to 1  $\mu\text{m}$  and alumina gel finished. Specimens were finally rinsed in ethanol–acetone binary mixture in ultrasonic bath, and dried.

Table 1: Composition (weight percent) of Alloy 690.

Ni	Cr	Fe	C	Co	Mn	Al	Ti	Cu	Si	S	P
59.31	29.20	9.94	0.018	0.014	0.31	0.13	0.270	<0.002	0.27	<0.0005	0.007

Some samples have been implanted with 180 keV  $\text{Xe}^+$  using the Van de Graaff accelerator at Laboratoire de Métallurgie Physique de Poitiers. The implantation is performed by focusing the beam and by sweeping it over the surface so that  $2 \times 10^{16}$  ions  $\text{cm}^{-2}$  were homogeneously implanted. The projected range ( $R_p$ ) and longitudinal straggling ( $\Delta R_p$ ) of 180 keV  $\text{Xe}^+$  ions calculated with the SRIM2008 code [10] are 28.8 nm and 10.8 nm in Alloy 690 ( $8.25 \text{ g cm}^{-3}$ ), respectively. The number of Ni, Cr and Fe vacancies induced by incident ion and per depth unit is calculated with SRIM as a function of depth (Figure 1). In this track region, the total vacancies concentration reaches 12.4 vacancies per implanted  $\text{Xe}^+$  per angstrom while the affected depth of alloy is approximately 50 nm. However, let us notice that SRIM does not take into account all recombinations and diffusion processes that could occur during and after implantation.

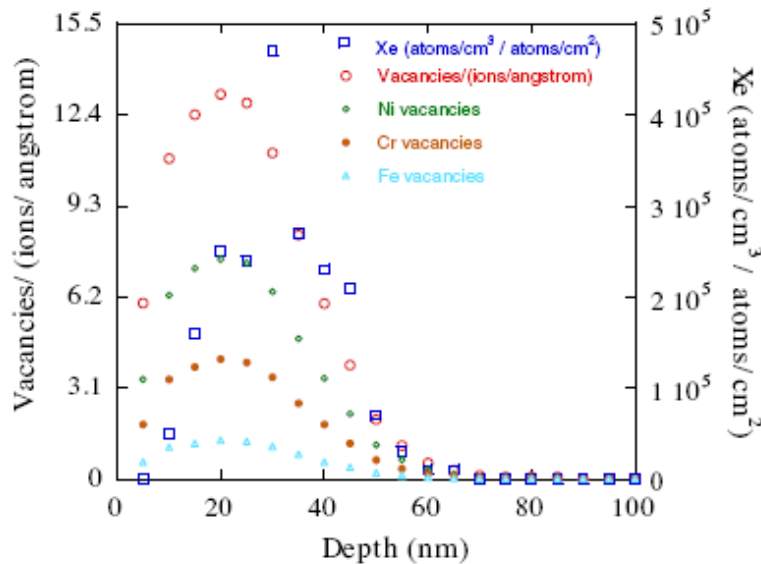


Figure 1: SRIM calculation of the vacancies and xenon concentrations as function of the depth in 180 keV  $\text{Xe}$ -implanted Alloy 690.

Ion implantation, known as proper material degradation tool, made thus possible to obtain a polished sample with a number of surface defects higher than simply-polished coupons, simulating hardening damage in Alloy 690.

## II.2. Corrosion experiments

In order to study the oxidation mechanism of  $\text{Xe}$ -implanted Alloy 690 in PWR primary coolant conditions, two different experiments have been implemented.

Kinetics experiments were carried out in a recirculation autoclave simulating primary water conditions, at  $325 \text{ }^\circ\text{C}$  under 155 bar. The aqueous solution contained  $2 \text{ mg L}^{-1}$  lithium and  $1000 \text{ mg L}^{-1}$  boron. A hydrogen overpressure of 0.29 bar was introduced to obtain a dissolved hydrogen concentration of  $1.3 \times 10^{-3} \text{ mol L}^{-1}$  and a low oxygen content ( $\text{O}_2 < 10 \text{ ppb}$ ). In this testing device, the pressurised hot water was continuously cleaned and purified to maintain the concentration of metallic cations at an extremely low level. Three different test durations were investigated to characterise the formation and the change in corrosion product scales on implanted samples: 88 h, 190 h and 304 h. In order to evaluate the role of surface defects on

oxidation kinetics, some non-implanted samples have also been corroded in the same conditions with various durations (24 h, 48 h, 66 h, 88 h, 112 h, 190 h, 304 h, 406 h, 858 h).

For understanding the transport mechanisms of oxygen through the corrosion product scales formed in the primary fluid on implanted samples, corrosion tests were also conducted in a sequential exposure under  $H_2(^{16}O)$  and  $H_2(^{18}O)$ . The first sequence was carried out in the same recirculation loop and with the same experimental conditions than the one previously described for kinetics experiments. The exposure times for this first sequence were either 88h (sample 1) or 190h (sample 2). The second cycle of corrosion was implemented in a Titanium autoclave for duration of 24 h in static conditions. The media was a mixed  $H_2(^{16}O)/H_2(^{18}O)$  aqueous solution corresponding to a ratio 80/20. The temperature, lithium, boron and hydrogen concentrations were the same than those used in the recirculation autoclave. Nevertheless, in this second device, no purification system is present. So a cationic saturation may be achieved in the autoclave. Consequently precipitation phenomena can take place which entail the growth of an external layer.

### II.3. Characterisation of the oxide scales

The corrosion product scales grown on Xe-implanted or non-implanted plates were analysed by several techniques (SEM, TEM, NRA, SIMS).

SEM have been made with a LEO 1450VP in order to study the morphology of the sample surface after corrosion treatments.

TEM characterisations were made on specimen cross-section. Before preparation, the sample was about 1 cm<sup>2</sup>. Two bars of about 2.5 mm width were cut along the plane of interest. Both bars were glued together with an epoxy resin, the surface of the oxide layers facing inwards so that it was protected from damage, forming a sandwich, which was then cut into slices of 0.5mm thickness. A slice was thinned mechanically to a thickness of 15-10  $\mu\text{m}$  using a precision tripod device in order to keep the sample absolutely horizontal. The sample was mounted onto a copper grid and thinned to a thickness of a few nanometres from both sides by low angles ( $\pm 7^\circ$ ) ion milling with 4 keV argon ions using a Gatan<sup>®</sup> Precision Ion Polishing System (PIPS). Final milling was performed at reduced beam energy (2 keV) and reduced incident angles ( $\pm 4^\circ$ ) to remove most of the visible ion damage. TEM investigations were carried out using a Tecnai F20 ST Field emission gun microscope, and equipped with an Energy-Dispersive X-ray (EDX) device, Gatan Imaging Filter (GIF) and Scanning Transmission Electron Microscopy (STEM) system. EDX analysis has been performed in line-scan mode to provide local chemical composition variation over oxide layers. High-resolution transmission electron microscopy (HRTEM) images were obtained using a CCD camera and analysed by Fourier technique to investigate structural and crystallographic details of the oxide layer.

NRA was hereby carried out to determine the oxide scale thickness formed on Ni-base samples after different exposure times to primary conditions. This technique is particularly sensitive, even for low element contents, with a nanometric depth resolution, and avoids the artefacts due to oxide etching. NRA experiments were performed at the Institut National des Sciences et Techniques Nucléaires (Saclay, France) using a Van de Graaff accelerator. Quantitative determination of <sup>16</sup>O content was made by considering the <sup>16</sup>O(d,p1)<sup>17</sup>O nuclear reaction analysis using a 900 keV deuteron beam. 1258 keV protons were collected at a backscattering angle of 150°. A Mylar stopping foil of 12  $\mu\text{m}$  was used to filter out the backscattered d<sup>+</sup>. Some references composed of a tantalum substrate surmounted by a Ta<sub>2</sub>O<sub>5</sub> oxide of well-known thicknesses were used to quantify oxygen.

SIMS analyses were executed on a CAMECA Riber MIQ256 system in order to characterise the oxygen isotope profiles in the oxide scale and in the underlying alloy. The spectrometer was run at an operating pressure of 10<sup>-9</sup> mbar. A 4 keV Ar<sup>+</sup> primary ion source was employed for analysis, delivering 5 nA of current over a 140  $\mu\text{m}$  × 200  $\mu\text{m}$  area. The incident angle was equal to 45°. The distribution of the following ions was achieved: <sup>16</sup>O<sup>-</sup>, <sup>16</sup>OH<sup>-</sup>, <sup>18</sup>O<sup>-</sup>, <sup>18</sup>OH<sup>-</sup>, <sup>52</sup>Cr<sup>+</sup>, <sup>56</sup>Fe<sup>+</sup>, <sup>58</sup>Ni<sup>+</sup>, <sup>104</sup>Cr<sub>2</sub><sup>+</sup> and <sup>130</sup>Xe<sup>+</sup>. Negative and positive ion profiles were recorded using the same analysis conditions. The sputtering time was converted into depth for the oxide by using

the thickness determined by NRA and by determining the interface oxide/metal with the inflexion point on the oxygen profile.

### III. Results

#### III.1. Morphological observations of implanted Alloy 690 specimens after corrosion tests

The microstructure of the oxide scales grown on implanted samples were characterised by two kinds of investigations: surfacic ones by scanning electron microscopy (SEM) and cross-sections ones by TEM and associated analytical techniques.

The change in morphology of oxide layers grown on Xe-implanted samples is presented on Figures 2a and 2b. These corrosion scales were obtained after 190 h and 304 h exposures to PWR conditions in dynamic non-saturated fluid. The essential characteristic of the surface morphology was the presence of numerous nanometric crystallites and few bigger crystallites (from 100 nm to 1  $\mu\text{m}$  size). Their morphology was polyhedral with a well-formed shape. After 190 h, the distribution of nanometric crystallites as well as their size seemed quite uniform. Nevertheless some areas on Figure 2a seemed to be free of crystallites. Whereas their surface density was more important after 304 h, the size of nanometric crystallites seemed to be independent of test durations. In comparison with observations performed on simply-polished samples (Figure 2c), the oxide scale hereby developed on defective surfaces did not present the same morphology even if the corrosion tests were conducted in similar conditions. The number of crystallites per unit of area was found to be higher in the case of implanted substrates.

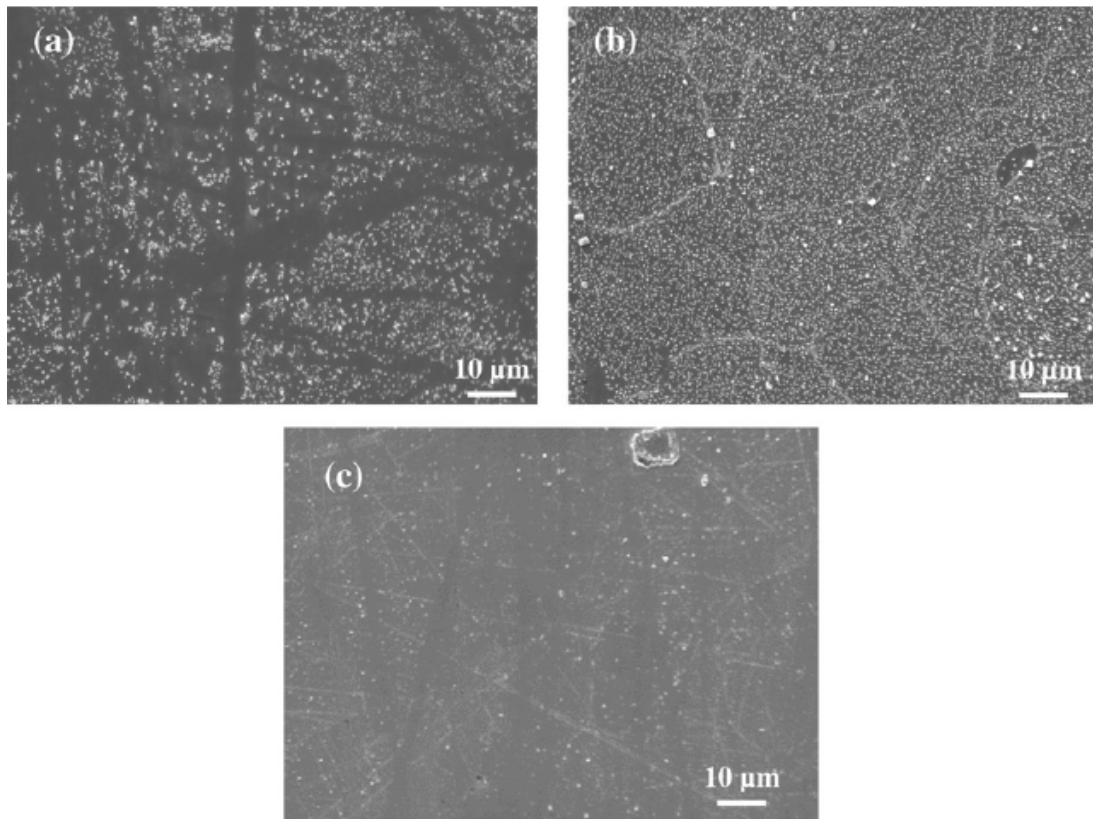


*Figure 2: SEM observations of the surface of Alloy 690, for both implanted and non-implanted samples, after different exposure times in PWR primary simulated conditions (325 °C) at optimised working conditions of the ion-exchange resins: Xenon-implanted ones after (a) 190 h and (b) 304 h; (c) non-implanted ones after 304 h.*

Concerning microstructural examination, the oxide layer formed on samples implanted with xenon and corroded during 304 h in PWR primary conditions were partly described previously [11]. Present TEM observations on specimen cross-sections confirmed that the damaged samples developed a duplex oxide structure similarly to the simply-polished Alloy 690

substrates. In Figure 3, comparison of the internal oxide layer between an implanted sample corroded for 304 h and a non-implanted one corroded for 858 h was conducted by using TEM images in the under-focused mode. Accurate microstructural observations highlighted differences in term of grain structures as well as oxide thicknesses. Thus the oxide formed on Xe-implanted alloys (Figure 3a) exhibited smaller grains or subgrains (only few nanometres, estimated to 5 nm) compared to the non-implanted one whose grains size was in the range of 15-20 nm (Figure 3b). As a consequence, the number of grains or subgrains boundaries per unit of area is higher in oxide scale formed on the defective materials. As for the thickness, it was obvious that the oxide scale grown on Xe-implanted samples was thicker than on the non-implanted substrate even if the exposure time was shorter (Figure 3).

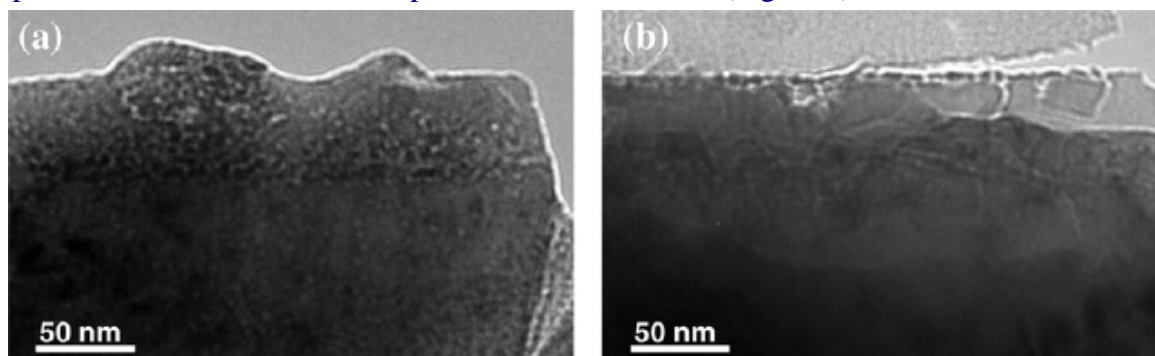


Figure 3: TEM comparison of the continuous oxide layers in under-focused mode obtained for the oxide layer developed (a) on Alloy 690 implanted with Xenon and exposed 304 h, and (b) on simply-polished Alloy 690 corroded for 858 h in PWR primary simulated conditions (325 °C).

Figure 4a shows a scanning TEM (STEM) image obtained in high angle annular dark field (HAADF) mode on the oxide film developed on Alloy 690 implanted with Xe<sup>+</sup> and exposed for 304 h. The contrast in this imaging mode is dominated by the atomic number Z of elements (Z-contrast), highlighting interfacial limit between oxide and matrix. The oxide scale exhibited a compact and polycrystalline aspect with a large density of structural defects. In order to investigate the chemical composition of the oxide layer, Energy-Dispersive X-ray (EDX) analysis using nanometric probe was performed in line-scan mode across this area, and chemical composition profiles summarised in Figure 4b confirmed the multi-scale oxide layer. The oxide composition was changing from the outermost surface to the bulk in such a way that it was possible to distinguish at least two sub-layers: an outer domain (10-15 nm in depth) richer in iron and an inner one enriched in chromium, compared to the continuous scale. These analyses also revealed chromium depletion below the oxide/alloy interface. Concerning the Xenon profile, this element was especially visible in the inner oxide scale, till a depth of about 100 nm. The experimental depth corresponding to the maximum of the Xe content, 50 nm, was closed to the one calculated using SRIM (30 nm) with an external layer estimated to 15 nm. The width of the implanted area was experimentally larger than previously calculated (Figure 1) since SRIM did not take into account all recombinations and diffusion processes that could occur during and after implantation. The microstructure of the internal oxide layer grown on Xe-implanted samples was extensively investigated by HRTEM as well as the interfacial area (Figure 4c). The internal oxide consisted in a continuous layer with dispersed nanometre-sized nodules at the oxide/alloy interface. The analysis of Fourier transforms (equivalent to electron diffraction patterns) of zones (e) and (d) revealed crystallographic distances and angles consistent with NiCr<sub>2</sub>O<sub>4</sub> and Cr<sub>2</sub>O<sub>3</sub> crystallographic structures respectively. However, EDX profile (Figure 4b) highlighted a composition of the continuous oxide layer consistent with nickel-iron mixed chromite Ni<sub>(1-x)</sub>Fe<sub>x</sub>Cr<sub>2</sub>O<sub>4</sub>. Even if such a structure had ever been observed for the oxide formed on the non-implanted Alloy 690 specimens [1], these new investigations illustrated the higher density of chromia particles as well as the apparition of a chromium depleted zone beneath the oxide scale when alloy surfaces were more defective.

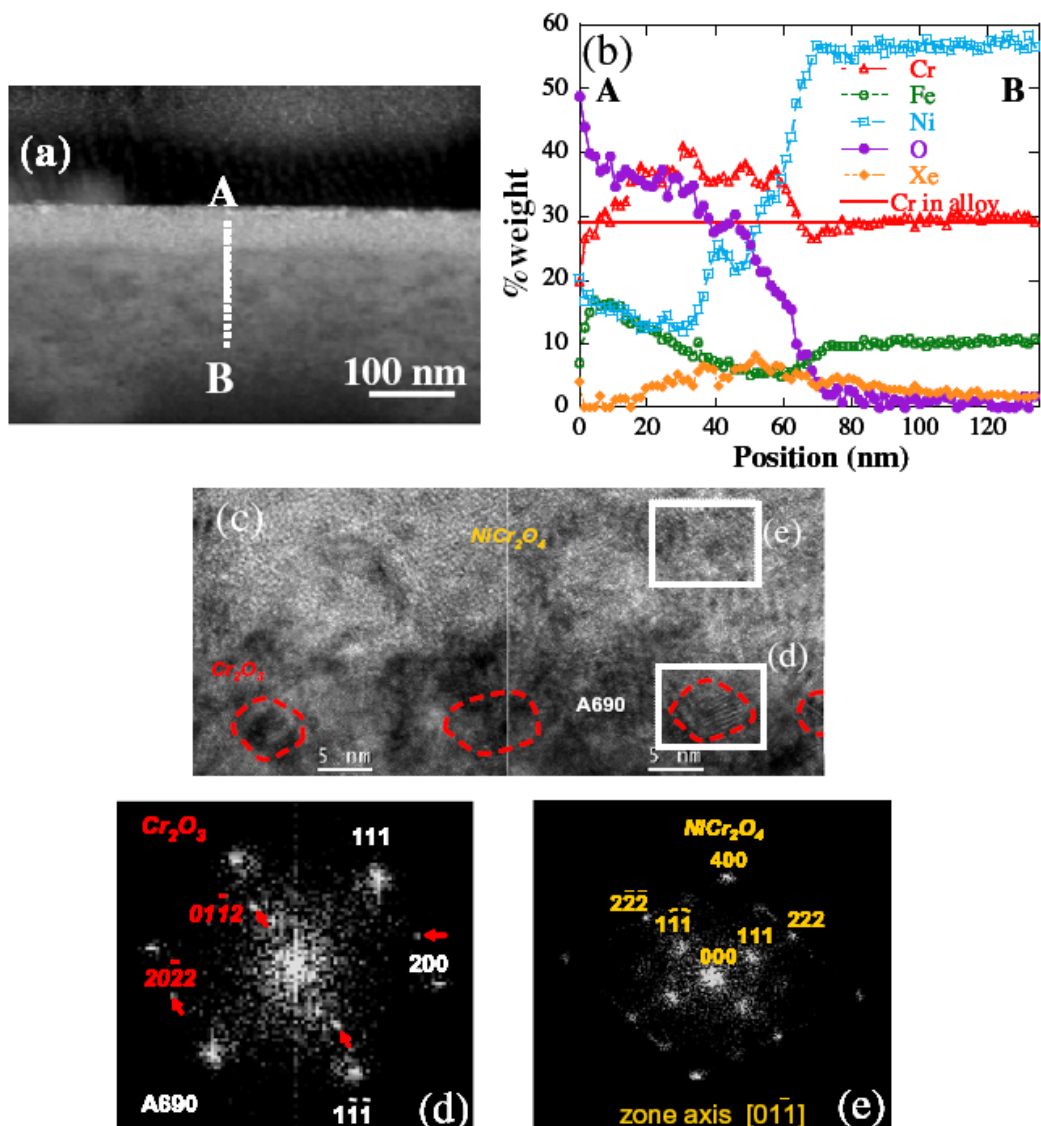


Figure 4: TEM cross-section analyses of the oxide film developed on Alloy 690 implanted with  $Xe^+$  and corroded 304 h in PWR primary simulated conditions: (a) dark field STEM image, (b) EDX compositional profiles obtained across the oxide layer and the underlying alloy using a nanometric electron probe, (c) HRTEM image. Presence of chromia nodules at the metal/oxide interface is evidenced (dashed lines), (d) and (e) Fourier transform diffractograms of the framed area on image establishing respectively the  $Cr_2O_3$  structure of the interfacial nodules and the  $NiCr_2O_4$  structure of the internal layer.

### III.2. Growth kinetics of oxide scales

From former microstructural observations, it was found that the oxide layer grown on Alloy 690 samples exposed to PWR conditions was nanometre thick. In such thickness range, NRA was an attractive alternative to XPS and SIMS in order to determine the concentration of oxygen since this ion beam technique is well adapted to such low elemental contents. From the particle energy spectra produced by 900 keV  $^2H^+$  beam, it was possible to determine oxygen content per surface unit considering the quantity of protons produced by the  $^{16}O(d,p)^{17}O$  nuclear reaction for instance.

An example of NRA spectra collected on the Xe-implanted sample exposed for 304 h to PWR primary conditions was plotted on Figure 5. This figure was only of high energy region corresponding to the positive Q-value nuclear reactions. The three registered peaks were assigned to  $^{16}O(d,p_0)^{17}O$ ,  $^{16}O(d,p_1)^{17}O$  and  $^{12}C(d,p_0)^{13}C$ . Both first ones correspond directly to  $^{16}O$  isotope, the last one results from the interaction between deuteron and carbon due to air

surface contamination. Quantification of oxygen in the surface layer was achieved with the most intense  $^{16}\text{O}(\text{d},\text{p}_1)^{17}\text{O}$  feature by using SIMNRA program [12]. This data was thereafter used to evaluate the oxide thickness, considering two major hypotheses: the oxide scale was uniform and compact, and it was composed of a single phase. However, according to the previous microstructural description (cf. Section III.2), both assumptions give a very simplified view of the oxide structure. Nevertheless, since the protective oxide scale is mainly made of nickel-iron mixed chromite, these simplifications are assumed to be consistent enough to evaluate the thickness, thanks to following equation:

$$e_{\text{eq}} = \frac{q \times (M_{\text{NiCr}_2\text{O}_4} + M_{\text{FeCr}_2\text{O}_4})}{4 \times (\rho_{\text{NiCr}_2\text{O}_4} + \rho_{\text{FeCr}_2\text{O}_4}) \times N_A} \quad (1)$$

where  $e_{\text{eq}}$  is the equivalent oxide layer thickness when compact and uniform,  $q$  the oxygen content per surface unit previously evaluated by NRA,  $N_A$  the Avogadro constant,  $M$  and  $\rho$  are the mass number and the density respectively of both spinels hereby considered for the calculation ( $\text{NiCr}_2\text{O}_4$  and  $\text{FeCr}_2\text{O}_4$ ).

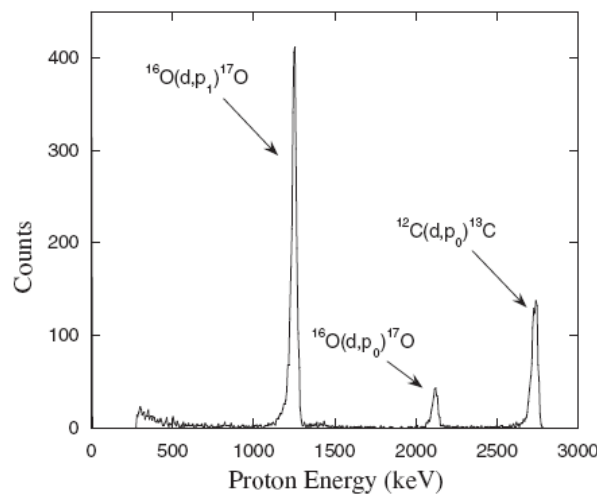


Figure 5: NRA spectrum recorded at room temperature with a 900 keV  $^2\text{H}^+$  incident beam on a  $\text{Xe}^+$ -implanted Alloy 690 exposed to PWR primary coolant conditions (325 °C) for 304 h.

Figure 6 shows the time dependent oxide thickness of implanted and non-implanted Alloys 690 exposed to PWR conditions. For both surface states, the thickness increases with increasing exposure time. Nevertheless, two tendencies can be distinguished depending on the initial surface state. The oxidation rate of the non-implanted alloy obeys a parabolic rate law. This behaviour is usually observed in high temperature oxidation when diffusion is supposed to be the limiting process [13].

The oxidation rate of the implanted samples follows a different behaviour: the initial period corresponds to rapid oxide formation. For longer exposure times, the slope drastically decreases, emphasising that oxide no longer progress significantly. This asymptotic-like behaviour corroborates the role played by surface defects on the kinetic behaviour. For the same exposure time, implanted samples developed a thicker oxide layer compared to the non-implanted ones, as illustrated by TEM examinations

### III.3. Oxygen transport throughout the oxide scale

Previous observations highlight morphological as well as kinetics effects of Xenon implantation on the oxide formation. In order to better understand the mechanism involved in this phenomenon, a two-stage isotopic oxidation treatment followed by SIMS analysis is well suited to such growth mechanism studies. Using this procedure, we are able to establish the region of old and new oxide growth as well as to determine oxygen transport paths [14] and [15] and/or the oxygen diffusion coefficient.  $^{18}\text{O}$  tracer experiments have been thus

performed by corroding samples of Ni-base alloy in corrosion loop and autoclave simulating the primary coolant.

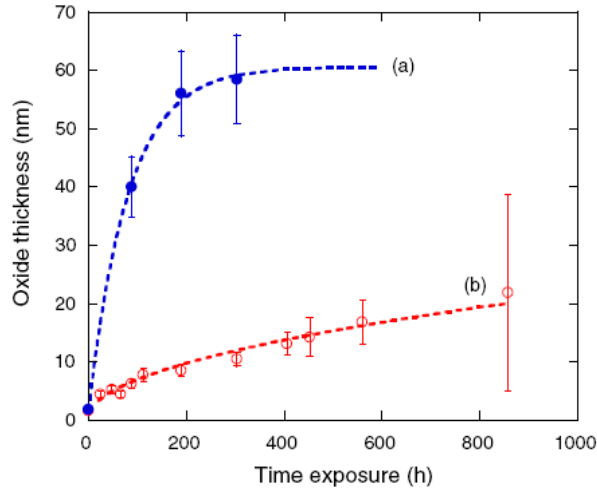


Figure 6: Time-dependent oxide scale thickness obtained on Alloy 690 (a) implanted or (b) simply polished after exposures to PWR primary simulated conditions in optimal working conditions. Thicknesses were evaluated from NRA  $^{16}\text{O}(d,p_1)^{17}\text{O}$  peak intensity. The experimental data were adjusted with (a) an asymptotic fit and (b) a parabolic law (dashed line).

In a previous work, we studied the oxygen transport through the protective oxide scale formed on simply-polished coupons of Alloy 690 during their exposition in PWR primary coolant conditions [16]. In this framework, we used a sequential exposure under media containing alternatively  $\text{H}_2(^{16}\text{O})$  and  $\text{H}_2(^{18}\text{O})$ , as described in Section II.2. of this article. The results reported in Reference [16] indicated that the oxygen transport through the oxide scale occurred by diffusion along the grain-boundaries network. An estimation of the value of oxygen diffusion coefficient  $D_{\text{SC}}^{\text{O}}$ , in the range  $2.10^{-18} \leq D_{\text{SC}}^{\text{O}} \leq 1 \times 10^{-17} \text{ cm}^2 \text{ s}^{-1}$ , was proposed. But, it is important to note that this estimation was rather rough due to a significant growth of the oxide scale during the second sequence.

So, the objective of the  $^{18}\text{O}$  tracers experiments conducted on implanted samples and presented in this paper is to obtain a better estimation of  $D_{\text{SC}}^{\text{O}}$ , by carefully limiting the growth during the second cycle of the sequential exposure.

In order to compare the  $^{16}\text{O}$  and  $^{18}\text{O}$  depth profiles with those published in literature [14] and [15], a mathematical treatment is used to plot data as if the experiments were performed in pure  $\text{H}_2(^{16}\text{O})$  or pure  $\text{H}_2(^{18}\text{O})$ . Indeed, the  $^{16}\text{O}$  intensity measured (noted  $I(^{16}\text{O})_{\text{B}}$ ) is the sum of the  $^{16}\text{O}$  intensities from the first sequence  $I(^{16}\text{O})_1$  and those of the second one  $I(^{16}\text{O})_2$ :

$$I(^{16}\text{O})_{\text{B}} = I(^{16}\text{O})_1 + I(^{16}\text{O})_2 \quad (2)$$

The  $^{18}\text{O}$  is only due to the second sequence so that the intensity is consistent with a composition of 20% and is proportional to  $I(^{16}\text{O})_2$  according to the following expression:

$$I(^{18}\text{O})_{\text{B}} = \frac{I(^{16}\text{O})_2}{4} \quad (3)$$

So the  $^{16}\text{O}$  and  $^{18}\text{O}$  intensities calculated as if the experiments were performed in pure  $^{16}\text{O}$  or pure  $^{18}\text{O}$  and noted  $I(^{16}\text{O})_{\text{R}}$  and  $I(^{18}\text{O})_{\text{R}}$  are obtained using the following expressions:

$$I(^{18}\text{O})_{\text{R}} = 5 \times I(^{18}\text{O})_{\text{B}} \quad (4)$$

$$I(^{16}\text{O})_{\text{R}} = I(^{16}\text{O})_{\text{B}} - 4 \times I(^{18}\text{O})_{\text{B}} \quad (5)$$

The oxygen profile obtained for the sequential test applied to Sample 2 was presented in Figure 7. The oxide/metal interface was estimated with the inflection point of the total oxygen profile (dashed line). The same mathematic treatment was applied to Sample 1 (not shown). The  $^{18}\text{O}$  distribution in the implanted samples exhibits an external accumulation zone followed by an inward diffusion.

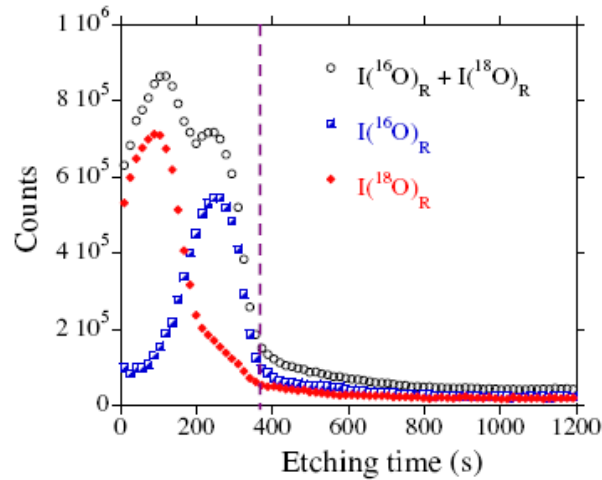


Figure 7: Mathematical treated depth profiles of  $^{16}\text{O}$  and  $^{18}\text{O}$  obtained by SIMS on Alloy 690 implanted with Xenon and exposed to a sequential corrosion test in PWR primary conditions (325 °C):  $\text{H}_2(^{16}\text{O})$  medium during 190 h, then in a mixed  $\text{H}_2(^{16}\text{O})/\text{H}_2(^{18}\text{O})$  medium during 24 h.

On the one hand, the oxygen inward diffusion leads to protective oxide layer growth [14], [15] and [16]. It can also be pointed out on Figure 7 that no significant accumulation of  $^{18}\text{O}$  at the oxide/alloy interface could be evidenced, contrarily to the case of previous experiments mentioned above [16]. This type of result is more favourable to make an evaluation of the oxygen diffusion coefficient. Indeed, in the present case, the growth of the internal scale is limited during the second sequence. Consequently, the experimental  $^{18}\text{O}$  depth profile in the internal scale seems to be more representative of a diffusion process than of a growth process and then could be studied as diffusion phenomena in semi-infinite medium [17].

On the other hand, the peak in the  $^{18}\text{O}$  profile, near the surface, reveals cationic processes: the oxide layer grows partly by outward diffusion and precipitation phenomenon. Indeed, previous investigations on the oxide scale morphology ever underlined that the protective oxide could be surmounted by a precipitated layer made of hydroxide and scattered octahedral crystals of mixed Ni/Fe ferrite, whose appearance depended on the media composition [1], [4], [11] and [18]. This result was coherent with the use of a static autoclave for the second sequence of oxidation, in which saturation in Ni and Fe cations was expected after long time exposure.

In order to better analyse the change in the positive species signals obtained by SIMS analyses, Cr/Ni and Cr/Fe ratios were evaluated. In Figure 8 are shown Cr/Ni and Cr/Fe ratios and the total oxygen profile corresponding to Sample 2. In the part near the surface, the profiles agree with the presence of nickel hydroxides or nickel ferrite; from the second part richer in chromium, it was assumed that the main compound in the inner layer was close to the  $\text{Ni}_{(1-x)}\text{Fe}_x\text{Cr}_2\text{O}_4$  chemical composition, as evidenced previously. Below the oxide/alloy interface, it was also possible to observe a plateau (Cr/Ni~12), hereby ascribed to the presence of chromia nodules at the alloy/oxide interface.

The oxygen concentration profiles can also be used to evaluate diffusion coefficients. The relative  $^{18}\text{O}$  concentration was first calculated from the ion intensities according to the formula  $[I(^{18}\text{O})_{\text{R}}/I(^{16}\text{O})_{\text{R}}+I(^{18}\text{O})_{\text{R}}]$ . On the representation of the  $^{18}\text{O}$  concentration as a function of the layer thickness (Figure 9), three domains could be identified. The domain (1)

corresponding to a constant  $^{18}\text{O}$  concentration is probably due to the growth of an external layer during the second sequence. The domain (2) corresponds to oxygen diffusion in the internal oxide scale. The last domain (3) is associated with a weak oxide growth at the alloy/oxide interface. As it was discussed before, the oxidation mechanism is driven by oxygen diffusion through the short circuits network (like grains boundaries). As a consequence, the oxygen concentration profile (Figure 9) in the internal oxide scale could be treated assuming that the oxygen diffusion process is governed by the C regime [17], [19] and [20], which describe diffusion phenomena in polycrystalline systems occurring along short circuits network at relatively low temperature (325 °C).

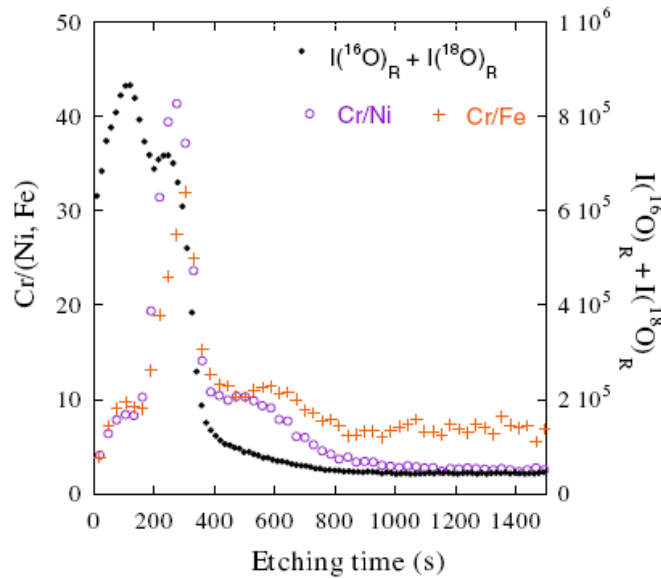


Figure 8: Total Oxygen depth profile, Cr/Ni and Cr/Fe intensities ratios obtained from SIMS analyses of Alloy 690 implanted with xenon and exposed to sequential isotopic corrosion tests (190 h + 24 h) in PWR primary conditions (325 °C).

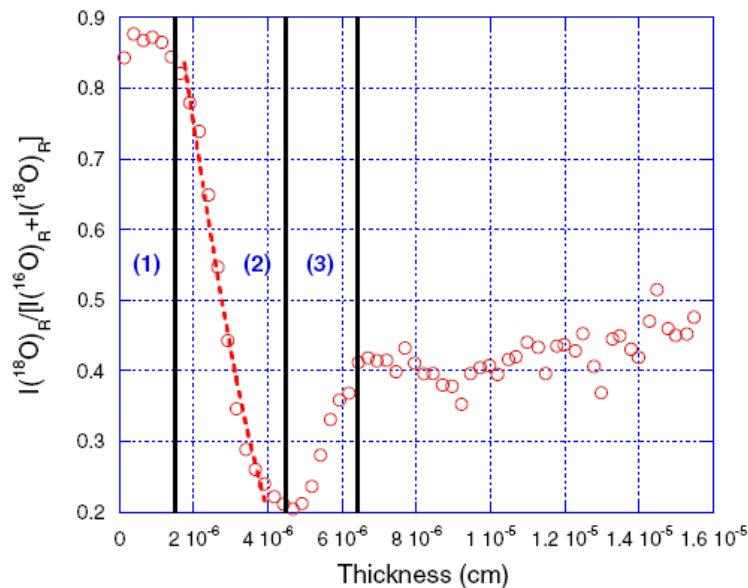


Figure 9: Plot of  $^{18}\text{O}$  concentration obtained from SIMS analyses of Alloy 690 implanted with xenon and exposed to sequential isotopic corrosion tests (190 h + 24 h) in PWR primary conditions (325 °C). The curve could be divided into three different domains: (1) growth of an external layer, (2) diffusion of  $^{18}\text{O}$  in the internal oxide scale and (3) weak accumulation of  $^{18}\text{O}$  at the oxide/alloy interface. The experimental data in the domain (2) were fitted with the Equation (9).

In order to fit the type of oxygen profile reported on Figure 9, the Equation (6) proposed by Mishin *et al.* [21], accounting an external growth of the oxide scale during the diffusion annealing was applied:

$$C(x) = K \times \operatorname{erfc}\left(\frac{x - \Delta x(t)}{2\sqrt{D_{sc}t}}\right) \quad (6)$$

where  $C(x)$  is the measured average concentration at the depth  $x$ ,  $\Delta x(t)$  is the thickness of the external scale formed during the second sequence (diffusion annealing) which lasted  $t$ ,  $D_{sc}$  is the short circuits diffusion coefficient and  $K$  is a constant proportional to the surface concentration and to the fraction of short circuits. Applying Equation (6) to oxygen profiles led to an estimation of the oxygen grain-boundary diffusion coefficients of  $2.0 \times 10^{-17} \text{ cm}^2 \text{ s}^{-1}$  and  $2.2 \times 10^{-17} \text{ cm}^2 \text{ s}^{-1}$  respectively for Samples 1 (not shown here) and 2 (Figure 9). These values seem to be more reliable than previous results discussed above, as regards to the limited growth of the internal oxide scale during the present diffusion annealing.

Finally, considering that  $\text{Ni}_{(1-x)}\text{Fe}_x\text{Cr}_2\text{O}_4$  is the main oxide in the protective oxide scale, the oxygen diffusion coefficient along grain boundaries  $D_{sc}^o$  in iron and nickel mixed chromite at 325 °C can be approximated to  $2 \times 10^{-17} \text{ cm}^2 \text{ s}^{-1}$ .

## IV. Discussion

Although oxidation of both Alloy 690 samples was performed in the same PWR primary conditions, Figure 6 clearly shows discrepancies on the oxidation curves depending on the surface state. Some disparities in morphology and oxygen transport were also noticed between both samples. This exhibits the role played by structural defects on the corrosion mechanism of Ni-base alloys. In order to understand the role of these structural defects, the oxide morphology differences will first be discussed, then the kinetic aspects of oxide growth will be addressed, on the basis of present results compared to literature data.

### IV.1. Duplex oxide layer

The oxide scale presents a duplex aspect with a Cr rich inner film and an outer one rich in Ni and Fe, as expected from previous analyses performed on Ni-base systems [3], [5] and [6]. More precisely, the protective oxide scale mainly consists of a continuous  $\text{Ni}_{(1-x)}\text{Fe}_x\text{Cr}_2\text{O}_4$  spinel layer surmounting chromia particles at the inner oxide/alloy interface, as already evidenced in former works [1] and [2]. From chemical profile analyses recorded after PWR primary exposures, xenon was located inside the internal oxide scale. This observation confirmed the prevailing anionic mechanism involving oxygen diffusion through the oxide [16]. Nevertheless, three main features could be distinguished between the implanted and the non-implanted samples.

- (1)  $\text{Cr}_2\text{O}_3$  nodules have been observed in the case of the oxide layer grown on simply-polished Alloy 690 but in lower density than in implanted samples [1]. This higher spatial occurrence of  $\text{Cr}_2\text{O}_3$  particles was ascribed to the higher defects density in the Xe-implanted samples, considered as preferential nucleation sites for oxide nodules. This hypothesis is also supported by the presence of a chromium-depleted underlayer (Figure 3b), which was not evidenced on simply-polished samples [1], and could be assigned to the more numerous  $\text{Cr}_2\text{O}_3$  nodules formation. Other authors mentioned the presence of a uniform and continuous chromia layer instead of dispersed particles [22], [23] and [24]. However such results were obtained on work-hardened or perturbed surfaces [22]. On another damaged surface state, Carrette *et al.* [3], [4] and [8] did not clearly conclude to the formation of a continuous chromia scale (these authors talked about a Cr rich oxide layer) but evidenced a large chromium depleted layer in the alloy under the oxide/alloy interface.

- (2) Concerning the continuous chromite layer, an increase of the surface defects density induces a decrease of the grain size as well as a thickening of the protective layer at the beginning of the corrosion process. The structural modifications in the protective oxide layer illustrate the influence of implantation damages on the oxide growth. Moreover, the growth of the spinel layer proceeds via grain-boundary diffusion of oxygen in the oxide and thus depends on the subsurface defects density.
- (3) The last difference concerns the presence of nanometric crystallites in the external layer which likely results from the precipitation on the specimen surface of Ni and Fe cations from the saturated corroding fluid. Even if very few of these precipitates were present on the surface of simply-polished samples when the ion-exchange resins worked in optimal conditions, their occurrence in the present study underlines that defects at the surface of the alloy also influenced the nucleation rate of the external layer.

#### IV.2. Growth mechanisms and kinetics

Chemical profile analyses corroborate previous conclusions about the internal growth mechanism of the protective oxide layer where oxygen is the main diffusing specie [16]. The diffusion of this specie through the internal oxide scale, mainly composed of  $\text{Ni}_{(1-x)}\text{Fe}_x\text{Cr}_2\text{O}_4$ , takes place along the grain boundaries of this oxide, which acts as a short circuits network. Morphological oxide layer description highlighted the high density of grain boundaries since the oxide grains were of nanometre size. Therefore, if the oxygen diffusion coefficient obtained for implanted samples is considered as a reasonable estimation of the oxygen diffusion coefficient along grain boundaries in iron and nickel mixed chromite at  $325^\circ\text{C}$  ( $D_{\text{sc}}^{\text{O}} \approx 2 \times 10^{-17} \text{ cm}^2 \text{ s}^{-1}$ ), the large discrepancy of short-circuits density, between implanted or not implanted samples, could explain the faster oxidation rate in Xe-implanted alloys. Indeed, the oxygen flux depends on the surface short-circuits density and as a consequence it is expected to be greater in the oxide formed on implanted samples due to the more numerous diffusion paths such as grains boundaries.

It has previously been evidenced that the growth kinetics of the protective oxide scale formed on simply-polished samples follows a parabolic law. Three other results reported in the literature, about the oxide layer grown of this type of substrate could be recalled:

- (i) the formation of this scale results from an internal growth mechanism [16],
- (ii) this oxide layer is mainly composed of  $\text{Ni}_{(1-x)}\text{Fe}_x\text{Cr}_2\text{O}_4$  [1] and
- (iii)  $\text{Ni}_{(1-x)}\text{Fe}_x\text{Cr}_2\text{O}_4$  formed in PWR primary conditions is a n-type semiconductor [2] so the point defects responsible for the growth seems to be in substitution in the anionic sublattice. Taking into account these considerations, the growth kinetics of this film could be governed, in first approximation, by the diffusion of oxygen in the oxide.

First it is assumed that (i) the fluxes are conservative and (ii) the reactive system satisfies the hypothesis of quasi-stationarity as stated by Sarrazin *et al.* [13]:

$$\frac{\partial C_{\text{V}}}{\partial t} = \frac{\partial J_{\text{V}}}{\partial x} \approx 0 \quad (7)$$

where  $t$  is the time,  $x$  is the position in the oxide scale and  $C_{\text{V}}$  and  $J_{\text{V}}$  are respectively the concentration and the flux of point defects responsible for the oxygen transport through the scale. In the following, these point defects are assumed to be oxygen vacancies, noted  $V_{\text{O}}^{\times}$  according to the Kröger-Vink notation [25]. The  $V_{\text{O}}^{\times}$  flux could then be described by the Equation (8):

$$|J_V| = \frac{f \times D_{SC}^{V_o^x}}{V_M} \times \frac{[V_o^x]_{(i)} [V_o^x]_{(e)}}{X(t)} \quad (8)$$

where  $D_{SC}^{V_o^x}$  is the diffusion coefficient of oxygen vacancies along grain boundaries,  $V_M$  is the molar volume of  $Ni_{(1-x)}Fe_xCr_2O_4$ ,  $X(t)$  is the thickness of the oxide scale and  $[V_o^x]_{(i)}$  and  $[V_o^x]_{(e)}$  are respectively the molar fraction of oxygen vacancies at the oxide/alloy and at the oxide/media interfaces.  $f$  is the surface fraction of atomic sites located in the short circuits network. For a polycrystalline material where grain-boundaries play the role of short circuits,  $f$  may be calculated from the relation  $f = 2\delta/\phi$  [13], with  $\delta$  the grain-boundary width and  $\phi$  the grain size. The growth kinetics of  $Ni_{(1-x)}Fe_xCr_2O_4$  per unit of area can then be described by the following rate equation:

$$\frac{1}{S} \frac{dn_{Ni_{(1-x)}Fe_xCr_2O_4}(t)}{dt} = \frac{1}{V_M} \frac{dX(t)}{dt} = \frac{|J_V|}{4} \quad (9)$$

where  $n_{Ni_{(1-x)}Fe_xCr_2O_4}$  is the amount of chromite formed at the time  $t$  on the surface  $S$ . Integrating Equation 9 yields the time dependence of the oxide thickness according to Equation (10) where  $X_0$  is the initial thickness of the oxide film:

$$X(t) = \sqrt{\frac{\delta \times D_{SC}^O}{\phi} \times t + (X_0)^2} \quad (10)$$

Provided that (i) the molar fraction of diffusive point defects, at their interface of consumption is neglected compared to the molar fraction at their interface of creation [13], and (ii) Equation (11), which relates the oxygen diffusion coefficient to the diffusion coefficient of the associated point defect is verified [13] and [26]:

$$D^O = D^{V_o^x} \times [V_o^x] \quad (11)$$

The experimental time dependent thicknesses obtained on simply-polished samples (curve b on Figure 6) were fitted with Equation (10). Considering an oxide grain size of roughly 15 nm (Figure 3) and a grain-boundary width of 1 nm [17], it results value of roughly  $1.9 \times 10^{-17} \text{ cm}^2 \text{ s}^{-1}$  for  $D_{SC}^O$ .

Even if the kinetics model proposed here, in order to describe the parabolic growth of the oxide scale formed on simply-polished Alloy 690, are very simplified, it is interesting to note that the value of  $D_{SC}^O$  obtained is in reasonable agreement with the value found by tracers experiments on Xe-implanted samples.

Nevertheless, the parabolic oxide growth observed here for the non-implanted samples by NRA measurements diverges from previous observations [3], [4], [22] and [24]. Carrette *et al.* [3] and [4] and Machet *et al.* [22] and [24] reported asymptotic and logarithmic growth respectively, which in fact are consistent with the experimental data obtained on Xe-implanted samples in this work (curve a on Figure 6).

These differences in the oxidation kinetics can be rationalised by considering the sample preparation and initial surface states. In previous mentioned studies, specimens used by Carrette *et al.* [3] and [4] were characterised by a thin polycrystalline outermost layer containing a lot of structural defects (like dislocations) while those used by Machet [22] prepared by hydraulic stamping were work-hardened. Considering the present results obtained on Xe-implanted Alloy 690, the oxidation kinetics can also be described by an

asymptotic law. Confrontation of all these data exhibits the role played by superficial defects in the corrosion kinetics. As formerly proposed, the initial high oxidation rate for implanted samples (or initially damaged substrates) compared to less defective samples would be due to a high density of grain boundaries. Since the oxidation rate is controlled by oxygen diffusion along the grain boundaries, the smaller the grains, the denser the network of grain boundaries, the faster the oxygen transport through the oxide layer. However, this feature cannot explain the rapid decrease in the oxidation rate for longer exposure times, which should involve a second mechanism as discussed hereafter.

For the formation of the Ni and Fe mixed chromite, as illustrated by Figure 10 which represents the alloy/oxide interface, two distinct interfaces must be considered: the spinel/alloy interface and the spinel/chromia one. Two mechanisms may thus contribute to the spinel formation. First, the mixed chromite oxide layer may be formed by direct oxidation of the metallic atoms of the Alloy A690. In this case, the oxidation takes place after the inward diffusion of oxygen through the oxide scale via grain boundaries as previously mentioned. The second possible mechanism would involve the interface between the chromia nodules and the mixed chromite spinel due to cations diffusion via the chromium oxide nodules. From literature data [27] and [28] extrapolated to PWR temperature conditions (325 °C), it can be assumed that the diffusion coefficients of Fe and Ni cations along the grain boundaries of  $\text{Cr}_2\text{O}_3$  ( $\alpha D_{\text{SC}}^{\text{Fe}} \approx 5 \times 10^{-23} \text{ cm}^2 \text{ s}^{-1}$  and  $\alpha D_{\text{SC}}^{\text{Ni}} \approx 3 \times 10^{-24} \text{ cm}^2 \text{ s}^{-1}$  referring respectively to References [27] and [28], where  $\alpha$  is the segregation factor) are significantly lower than the grain boundaries diffusion coefficient of oxygen in mixed chromite. However, when the density of  $\text{Cr}_2\text{O}_3$  nodules becomes significant, the cations diffusion via chromia nodules probably becomes the rate-controlling step of the growth of mixed chromite. Since the density of nodules at the oxide/alloy interface increases with the amount of subsurface defects, the important decrease in the oxidation rate for longer exposure times appears to be due to a change in the rate-limiting step from oxygen grain boundaries diffusion in the mixed chromite to cationic diffusion through more and more numerous  $\text{Cr}_2\text{O}_3$  nodules.

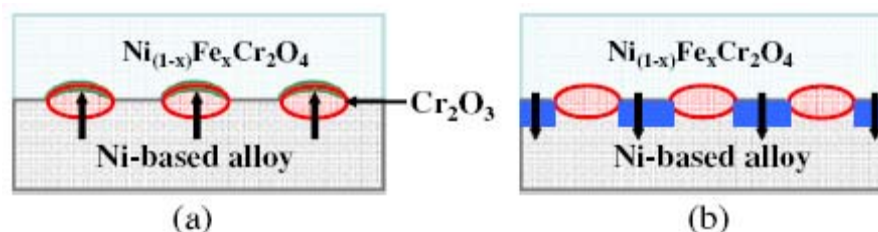


Figure 10: Schematic description of the two mechanisms assumed to contribute to the spinel formation. (a) Outwards cationic diffusion through chromia particles. (b) Inwards oxygen diffusion through the oxide scale.

On the contrary, for simply-polished samples, the parabolic growth of oxide scale could be the consequence of a low density of subsurface defects in the alloy. In this case, few nodules of  $\text{Cr}_2\text{O}_3$  appear at the alloy/oxide interface without any significant consequence on the oxidation kinetics. The growth of the mixed chromite was then only limited by the diffusion of oxygen into the oxide layer, at least at the experimental time scale.

## V. Conclusion

The influence of subsurface defects, generated by xenon implantation, on the generalised corrosion of Nickel-base alloys in PWR primary conditions was investigated.

From TEM observations, it was shown that defects at the alloy surface played a strong role on oxides nucleation processes, inducing structural modifications in the subsequent oxide scale.

- (1) The density of the nanometre-sized chromia nodules at the oxide/alloy interface largely increased.
- (2) The internal continuous mixed chromite layer was characterised by a smaller grain size, entailing a higher grain boundaries concentration as well.

- (3) These structural modifications in the internal oxide scale had thereafter consequences on the oxidation kinetics.
- (4) At the beginning of the corrosion process, the oxide layer thickness increased largely quicker on the damaged surface. This phenomenon is likely due to an increase of the inward oxygen diffusion at the grain boundaries of the continuous mixed chromite layer.
- (5) Then the strong decrease of the oxidation rate observed for longer exposure times in the damaged materials could be associated to a second mechanism for the spinel growth. This one requires outward cations (Fe, Ni) diffusion through Cr<sub>2</sub>O<sub>3</sub> nodules, which is a slower process compared to inwards oxygen diffusion through the continuous mixed chromite layer.

Ongoing research based on these first observations aiming to improve our understanding of the effects of subsurface damages on these corrosion processes is currently carried out, by varying the implantation conditions (such as fluencies and energies) in order to get a large panel of damaged structures.

### Acknowledgements

The authors would like to thank Michel Drouet from the Laboratoire de Métallurgie Physique of Université de Poitiers for performing Xe implantation, Olivier Heintz and Sébastien Chevalier from the Laboratoire de Recherches sur la Réactivité des Solides of Université de Bourgogne for SIMS experiments as well as Stéphanie Pellegrino and Sylvain Vaubaillon from the Laboratoire Van de Graaff of INSTN/CEA for NRA measurements.

### References

- [1] M. Sennour, L. Marchetti, F. Martin, S. Perrin, R. Molins and M. Pijolat. *J. Nucl. Mater.*, 402 (2010), pp. 147-156.
- [2] L. Marchetti, S. Perrin, Y. Wouters, F. Martin and M. Pijolat. *Electrochim. Acta*, 55 (2010), pp. 5384-5392.
- [3] F. Carrette, Relâchement des produits de corrosion des tubes en alliage 690 de générateur de vapeur du circuit primaire des réacteurs d'eau pressurisée Thesis, Institut National Polytechnique de Toulouse, France, 2002.
- [4] F. Carrette, M.C. Lafont, L. Legras, L. Guignard and B. Pieraggi. *Mater. High Temp.*, 20 (2003), pp. 581-591.
- [5] J. Panter, B. Viguier, J.-M. Cloué, M. Foucault, P. Combrade and E. Andrieu. *J. Nucl. Mater.*, 348 (2006), pp. 213-221.
- [6] F. Delabrouille, B. Viguier, L. Legras and E. Andrieu. *Mater. High Temp.*, 22 (2005), pp. 287-293.
- [7] L. Guinard, O. Kerrec, S. Gardey, D. Noel, Investigations for Reducing the Release of Steam Generator Materials: Experiments and Modelling, JAIF (Japan Atomic Industrial Forum) International Conference on Water Chemistry in Nuclear Power Plants, Niigata (Japan), 1998.
- [8] F. Carrette, L. Guinard, B. Pieraggi, Kinetics of Corrosion Products Release from Nickel-base Alloys Corroding in Primary Water Conditions: a New Modelling of Release, International Conference on Water Chemistry in Reactors Systems, Avignon, France, 2002
- [9] E. Moleiro, F. Carrette, J. M. Boursier, L. Legras, L. Guinard, Electropolishing Steam Generator Tubing: a Promising Way to Reduce Dose Rates and Mitigate AOA, International Conference on Water Chemistry in Reactors Systems, San Francisco, USA, 2004.
- [10] J.F. Ziegler and J.P. Biersack, *The Stopping and Range of Ions in Solids*, Pergamon Press, New York (1985).

- [11] M. Sennour, L. Marchetti, S. Perrin, M. Pijolat and O. Raquet. *Mat. Sci. Forum*, 595-598 (2008), pp. 539-547.
- [12] M. Mayer, SIMNRA users guide, Technical Report IPP 9/113, 1997. Available on <<http://www.rzg.mpg.de/~mam/>>.
- [13] P. Sarrazin, A. Galerie and J. Fouletier, *Mechanisms of High Temperature Corrosion: a Kinetic Approach*, Trans Tech Publications Ltd., Zurich, Switzerland (2008).
- [14] S. Chevalier, G. Strehl, J. Favergeon, F. Desserrey, S. Weber, O. Heintz, G. Borchardt and J.P. Larpin. *Mater. High Temp.*, 20 (2003), pp. 253-259.
- [15] S.N. Basu and J.W. Halloran. *Oxid. Met.*, 27 (1987), pp. 143-155.
- [16] L. Marchetti, S. Perrin, O. Raquet and M. Pijolat. *Mat. Sci. Forum*, 595-598 (2008), pp. 529-537.
- [17] J. Philibert, *Atom movements Diffusion and Mass Transport in Solids*, Les Editions de physique, Les Ulis, France (1991).
- [18] A. Machet, A. Galtayries, P. Marcus, P. Combrade, P. Jolivet and P. Scott. *Surf. Interface Anal.*, 34 (2002), pp. 197200.
- [19] L.G. Harrison. *Trans. Faraday Soc.*, 57 (1961), pp. 1191-1199.
- [20] Y.M. Mishin, C. Herzig, J. Bernardini and W. Gust. *Int. Mater. Rev.*, 42 (1997), pp. 155-178.
- [21] Y.M. Mishin and G. Borchardt. *J. Phys. III*, 3 (1993), pp. 863-881.
- [22] A. Machet, *Etude des premiers stades d'oxydation d'alliages inoxydables dans l'eau à haute température*, Thesis, Université Pierre et Marie Curie, Paris VI, France, 2004.
- [23] A. Machet, A. Galtayries, S. Zanna, L. Klein, V. Maurice, P. Jolivet, M. Foucault, P. Combrade, P. Scott and P. Marcus. *Electrochim. Acta*, 49 (2004), pp. 3957-3964.
- [24] A. Machet, A. Galtayries, P. Jolivet, M. Foucault, P. Combrade, P. Scott and P. Marcus, in: D. Féron, J.-M. Olive, Editors, *Corrosion issues in light water reactors: stress corrosion cracking (EFC 51)*, Woodhead Publishing Limited, Cambridge, United Kingdom (2007).
- [25] F.A. Kröger and H.J. Vink. *Solid State Physics*, 3 (1956), pp. 307-435.
- [26] M. Soustelle, *Heterogenous Kinetics Handbook*, John Wiley & Sons, Hoboken, USA (2010).
- [27] A.C.S. Sabioni, A.M. Huntz, F. Silva and F. Jomard. *Mater. Sci. Eng.*, A392 (2005), pp. 254261.
- [28] A.C.S. Sabioni, A.M. Huntz, J.N.V. Souza, M.D. Martins and F. Jomard. *Philos. Mag.*, 88 (2008), pp. 391-405.